Evaluating the Effective Segregation Coefficient in High-Purity Germanium (HPGe) Crystals for Ge Detector Development in Rare-Event Searches

S. Chhetri a , D.-M. Mei a,1 , S. Bhattarai a , N. Budhathoki a , A. Warren a , K.-M. Dong a , S.A. Panamaldeniya a , A. Prem a

^aDepartment of Physics, University of South Dakota, 414 E. Clark Street, Vermillion, South Dakota, 57069, USA

E-mail: dongming.mei@usd.edu

ABSTRACT: The performance and scalability of rare-event physics experiments depend on large-volume, detector-grade high-purity germanium (HPGe) crystals with precise control of impurity segregation during growth. We report a detailed study of impurity distribution in a single Czochralski-grown HPGe crystal produced at USD. The crystal was sectioned longitudinally into 37 segments, enabling the first high-resolution and systematic mapping of dopant profiles along the length of a detector-grade HPGe boule. Hall-effect measurements were used to extract impurity concentrations for boron (B), aluminum (Al), gallium (Ga), and phosphorus (P) in each segment. From these data, we determine effective segregation coefficients ($K_{\rm eff}$) and initial melt concentrations (C_0) for the dominant dopants and compare them with classical Burton–Prim–Slichter expectations. The results provide quantitative insight into impurity transport and melt–solid partitioning under realistic detector growth conditions. These findings inform process-optimization strategies for HPGe crystal pulling, improve impurity control along the boule, and support the reliable fabrication of large, low-background HPGe detectors for next-generation rare-event searches.

KEYWORDS: HPGe Crystal Growth, Hall Effect, Detector, Rare-event Physics

¹Corresponding author.

C	contents				
1	1 Introduction				
2	Experimental Procedures	3			
3	Characterization				
	3.1 Methodology	6			
4	Results and Discussion	7			
	4.1 Boron and Phosphorus Segregation	8			
	4.2 Aluminum and Gallium Segregation	8			
	4.3 Uncertainty Analysis	10			
	4.4 Comparison with BPS Model and Literature	11			
5	Conclusion	13			

1 Introduction

Dark matter and neutrinos are among the most abundant yet least understood constituents of the universe. High-purity germanium (HPGe) detectors, with net impurity concentrations at the level of ~ 10^{10} cm⁻³, have become key technologies for probing physics beyond the Standard Model, including dark-matter interactions and neutrinoless double-beta decay [1–8]. Early germanium-based experiments such as CoGeNT [9], which reported a possible dark-matter signal, and KKDC [10], which claimed evidence for neutrinoless double-beta decay, helped establish Ge as a leading target for rare-event searches. More sensitive experiments, including SuperCDMS, EDELWEISS and CDEX [11–13], have since ruled out the CoGeNT-favored parameter space, yet Ge detectors still provide state-of-the-art sensitivity for dark-matter masses below a few GeV/c². In the double-beta decay sector, GERDA and MAJORANA [14, 15] have refuted the KKDC claim using large arrays of ultra-low-background HPGe detectors.

Building on these advances, the LEGEND program [16] aims at a ton-scale search for neutrinoless double-beta decay using enriched HPGe. At the same time, leading dark-matter experiments in the GeV mass range, such as SuperCDMS [17], LUX-ZEPLINE (LZ) [18] and XENONnT [19], continue to push direct-detection limits. Recently, the Germanium-based Quantum Sensors for Low-Energy Physics (GeQuLEP) platform has been proposed, in which cryogenic (4 K) phonon spectroscopy with HPGe enables sensitivity to MeV-scale dark matter [20, 21]. In all of these efforts, the sensitivity of Ge-based experiments depends critically on the availability of large-volume, detector-grade HPGe crystals with well controlled impurity content and uniformity.

Increasing the HPGe crystal diameter beyond 4 inches enhances rare-event sensitivity, especially for weakly interacting massive particles (WIMPs). However, crystals grown at the Earth's

surface without adequate shielding are exposed to cosmic rays that produce long-lived cosmogenic isotopes in the crystal volume. These isotopes contribute to background events and degrade both detector sensitivity and energy resolution. To mitigate such effects, the entire production chain – zone refining, crystal growth and detector fabrication – should ideally be carried out in an underground environment, where the cosmic-ray flux is strongly suppressed [22]. While underground crystal growth is technically and logistically challenging, it is a key step toward achieving the ultra-low-background HPGe detectors required for next-generation dark-matter and neutrinoless double-beta decay experiments.

Detector-grade HPGe crystals are typically produced through a sequence of highly controlled steps [23–25]. Raw Ge is first purified by zone refining [26], then further purified during Czochralski (CZ) crystal pulling, and finally characterized by Hall-effect measurements before detector fabrication [27]. A high-purity hydrogen atmosphere during zone refining and crystal growth is essential [23, 24] to suppress electrically active impurities. Detector-grade quality further requires dislocation densities in the range $3 \times 10^2 - 1 \times 10^4$ cm⁻², so that charge trapping by di-vacancy–hydrogen complexes (V_2 H) is minimized, and a net impurity concentration of order 10^{10} cm⁻³ with good homogeneity throughout the volume [28, 29]. Dislocation-free Ge crystals up to 30 cm in diameter can be grown in inert atmospheres using resistance heating and graphite crucibles [30]. In contrast, CZ growth from ultra-pure quartz crucibles in high-purity hydrogen with radio-frequency induction heating offers improved thermal-field uniformity and strong melt convection, but also introduces additional challenges: reactions between molten Ge and quartz can create oxygen-related complexes that act as trapping centers, and ambient hydrogen can form V_2 H complexes that degrade charge collection [31].

Impurity segregation during zone refining and CZ growth is governed by the equilibrium distribution coefficient $K_0 = C/C_0$, defined as the ratio of the solute concentration in the solid (C) to that in the liquid (C_0) [32, 33]. For HPGe, the dominant electrically active impurities are boron (B), aluminum (Al), gallium (Ga) and phosphorus (P). Their segregation behavior controls how these dopants are distributed along the length of the ingot or crystal: species with K > 1 concentrate near the head, while those with K < 1 accumulate near the tail [25, 26, 28]. In practical growth conditions, however, convection, incomplete mixing and finite growth rates lead to effective segregation coefficients K_{eff} that can differ significantly from the equilibrium values. Accurate knowledge of K_{eff} under realistic detector-growth conditions is therefore essential for predicting impurity profiles and optimizing HPGe crystal pulling.

The University of South Dakota (USD) has produced HPGe crystals using the Czochralski technique for several decades and has developed the capability to fabricate radiation detectors with various geometries from these crystals [34–36]. In the present work, a single detector-grade HPGe crystal grown at USD was longitudinally sectioned into 37 segments to obtain a high-resolution map of impurity distribution along the boule. Using Hall-effect measurements, we extract impurity concentrations for B, Al, Ga and P in each segment and determine the corresponding effective segregation coefficients K_{eff} and initial melt concentrations C_0 . To our knowledge, this is the first systematic, high-resolution longitudinal study of impurity segregation in a single HPGe crystal grown under realistic detector conditions at USD. The Czochralski growth chamber used in this work is shown in Fig. 1; the methodology and results of the impurity-distribution analysis are presented in the following sections.



Figure 1. Czochralski crystal growth chamber used at USD for high-purity germanium crystals under controlled thermal and atmospheric conditions.

2 Experimental Procedures

At USD, raw germanium with an initial impurity concentration of $\sim 10^{14}~\rm cm^{-3}$ is first purified by a multi-pass zone-refining process. After 14 passes, the net carrier concentration is reduced to $\sim (10^{11} - 10^{12})~\rm cm^{-3}$ as measured by Hall-effect characterization at liquid-nitrogen temperature (77 K). The purified material is then loaded into a high-purity quartz crucible, 18 cm in diameter and 11 cm in depth, for subsequent Czochralski (CZ) growth [26, 37].

Before each growth run, a rigorous cleaning protocol is implemented to minimize contamination. The Ge ingots are rinsed with deionized (DI) water and acetone to remove organic residues, followed by a DI water rinse and a mixed-acid etch in nitric and hydrofluoric acids in a (3:1) HNO₃:HF ratio to remove surface-bound impurities. The quartz crucible and radiation shields are cleaned with H_2O_2 and dried with high-purity nitrogen gas [28]. The inner surfaces of the growth chamber (Fig. 1) are also wiped and inspected to ensure that residues from previous runs are removed, providing a clean environment for detector-grade crystal growth.

A total of 4905 g of purified Ge is charged into the quartz crucible, which is placed on an ultrapure graphite susceptor that converts radio-frequency (RF) power into heat. The charge is melted by applying ~ 12.5 kW of continuous RF power for about 2 h. During this stage, the chamber is first evacuated with a mechanical pump and then with a diffusion pump, improving the pressure from (6-7) Pa down to $(1-2) \times 10^{-3}$ Pa. After evacuation, 5N-purity hydrogen is introduced at a flow rate of 150 L/h and a pressure of 1 atm, and the atmosphere is maintained under these conditions throughout growth.



Figure 2. Schematic of the main stages of Czochralski growth for HPGe: (a) neck formation, (b) shoulder expansion, and (c) constant-diameter body growth.

Once the melt is fully established, a $\langle 100 \rangle$ -oriented HPGe seed is dipped into the melt and pulled to form the neck. The crystal is rotated at 3 rpm. The pulling rate is maintained at 40 mm/h during necking to suppress dislocations and then reduced to 20 mm/h for shoulder enlargement and constant-diameter body growth, as illustrated in Fig. 2. After melting, the RF power is gradually reduced to about 9.5 kW and subsequently adjusted to maintain the desired crystal diameter and a stable solid–liquid interface. Particular care is taken in the final stage of growth to avoid leaving residual molten Ge in the crucible, which can impose excessive thermal stress and crack the quartz.

Upon completion of the pull, a controlled automated cool-down of ~ 10 –11 h is used to bring the system back to room temperature and to minimize thermal stress in both crystal and crucible.

The resulting $\langle 100 \rangle$ HPGe crystal, shown in Fig. 3, has a diameter of approximately 8 cm near the shoulder, expanding to about 11 cm toward the tail, and is then removed from the chamber for slicing and subsequent characterization.

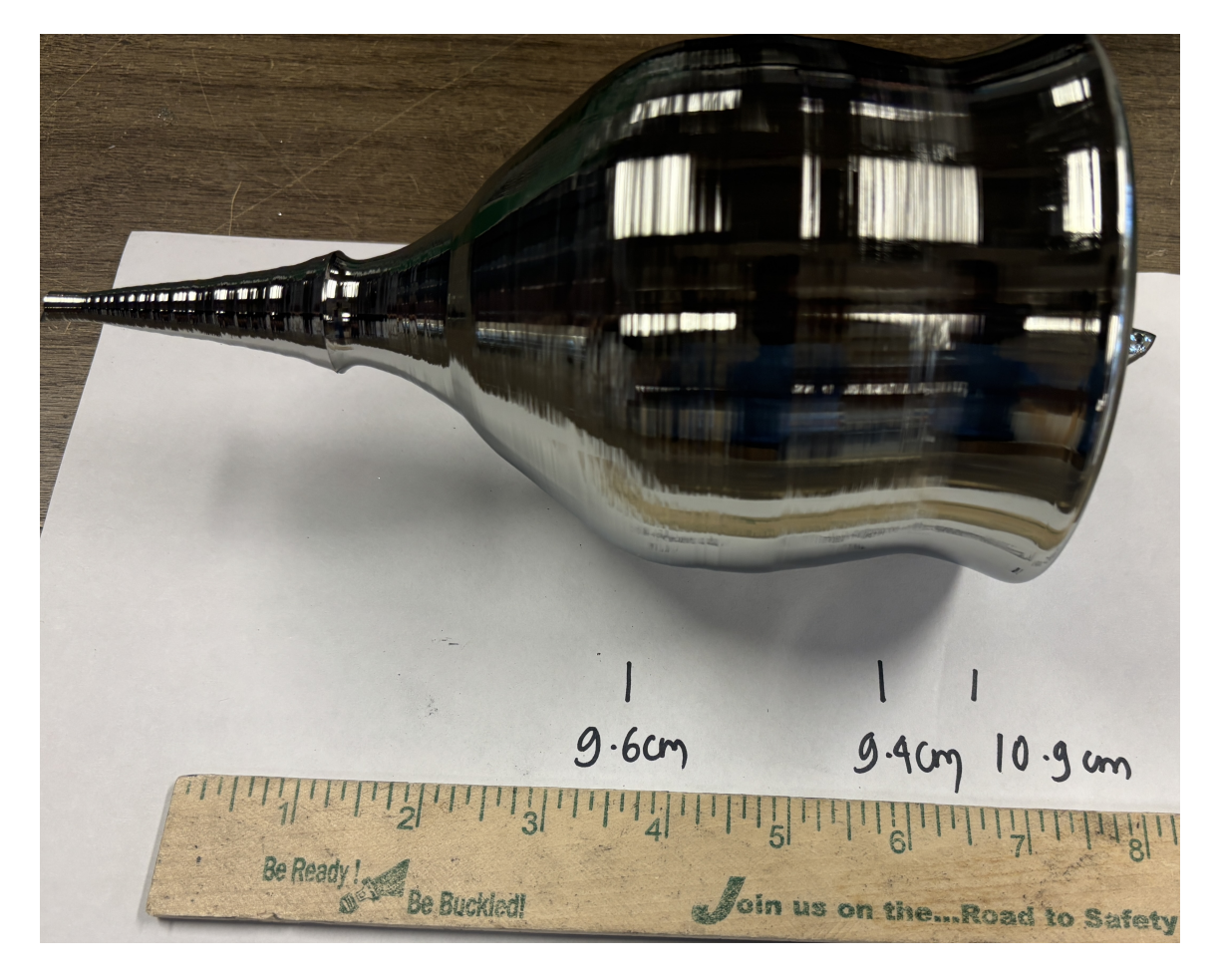


Figure 3. HPGe crystal grown at USD using the Czochralski technique. The diameter is ~ 8 cm near the shoulder and increases to ~ 11 cm toward the tail region.

3 Characterization

The single HPGe crystal was longitudinally sectioned into 37 segments to obtain a high-resolution impurity profile along the boule, as shown in Fig. 4. Sectioning was performed with a diamond wire saw, after which each segment was trimmed to the required dimensions using a water-cooled saw and finished on a lapping wheel to achieve flat, uniform surfaces suitable for electrical characterization.

Ohmic contacts were formed at the four corners of each sample using a gallium-indium eutectic alloy (Ga:In = 75.5:24.5 by weight, stored under argon atmosphere). The samples were then annealed at 360° C for ~ 1 h to promote alloy infiltration and ensure a stable, low-resistance interface with the Ge surface. This thermal treatment does not alter the near-surface properties of HPGe, and previous studies [27] have shown that such contact formation does not bias Hall-effect

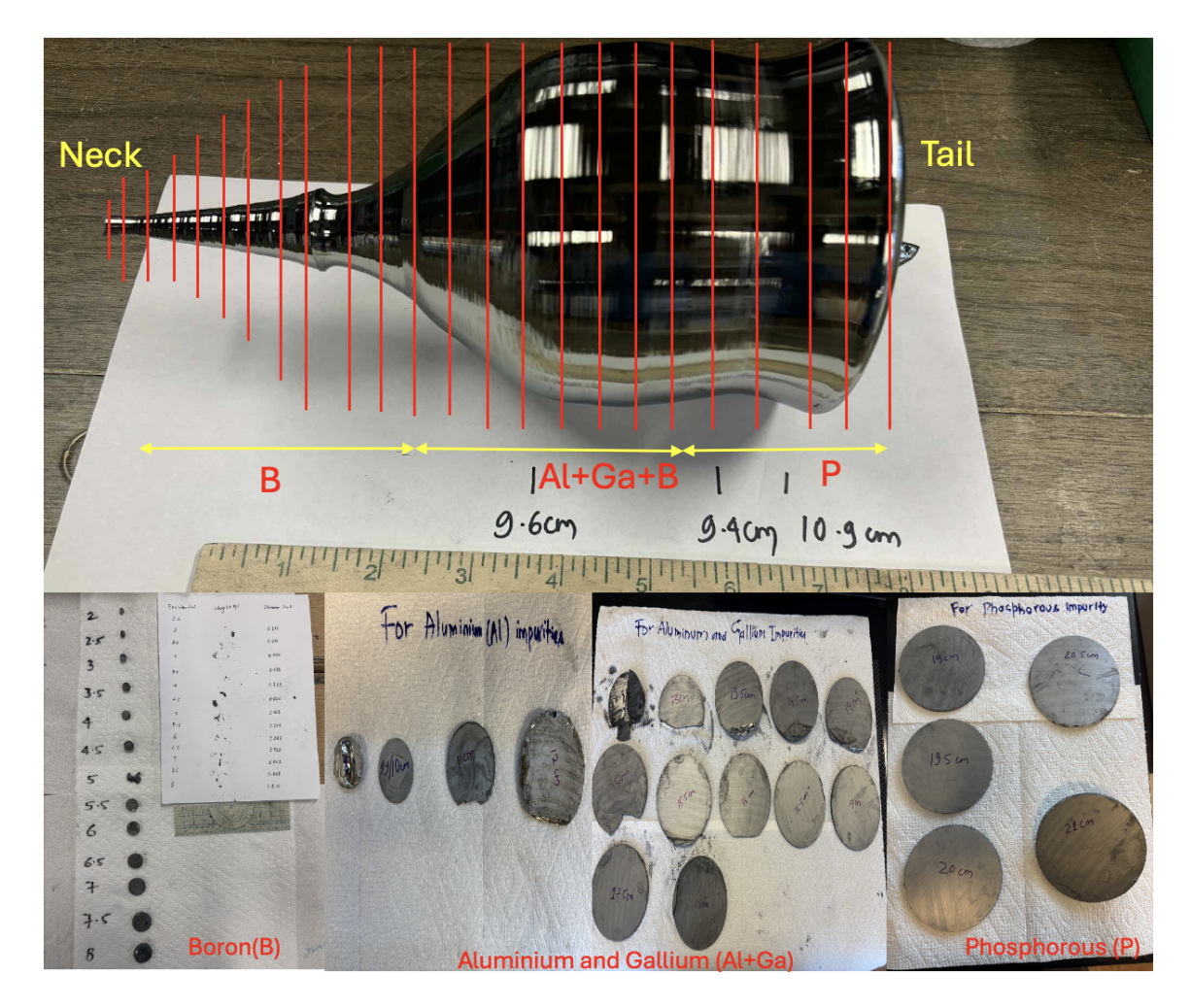


Figure 4. Impurity distribution along the length of the HPGe crystal grown at USD. Red vertical lines mark the positions where the crystal was longitudinally sectioned into 37 segments using a diamond wire saw for Hall-effect characterization. The profile shows strong boron dominance in the first ~ 15 cm of the crystal.

measurements. Net impurity concentrations were measured at liquid-nitrogen temperature (77 K) in a 0.55 T magnetic field using an Ecopia HMS-3000 Hall-effect system (Fig. 5).

Guided by the known equilibrium segregation behavior of the dominant impurities [38], we interpret the longitudinal profile in Fig. 4 as follows. Boron is expected to dominate in the first ~ 9 cm of the crystal, with the combined aluminum and gallium contribution extending out to ~ 15 cm. Phosphorus becomes significant only in the later portion of the boule, primarily beyond ~ 15.5 cm toward the tail. These regions inform our extraction of effective segregation coefficients for B, Al+Ga, and P.

3.1 Methodology

The variation of impurity concentration along the crystal during CZ growth can be described by [39]

$$C = C_0 K_{\text{eff}} (1 - g)^{K_{\text{eff}} - 1}, \tag{3.1}$$

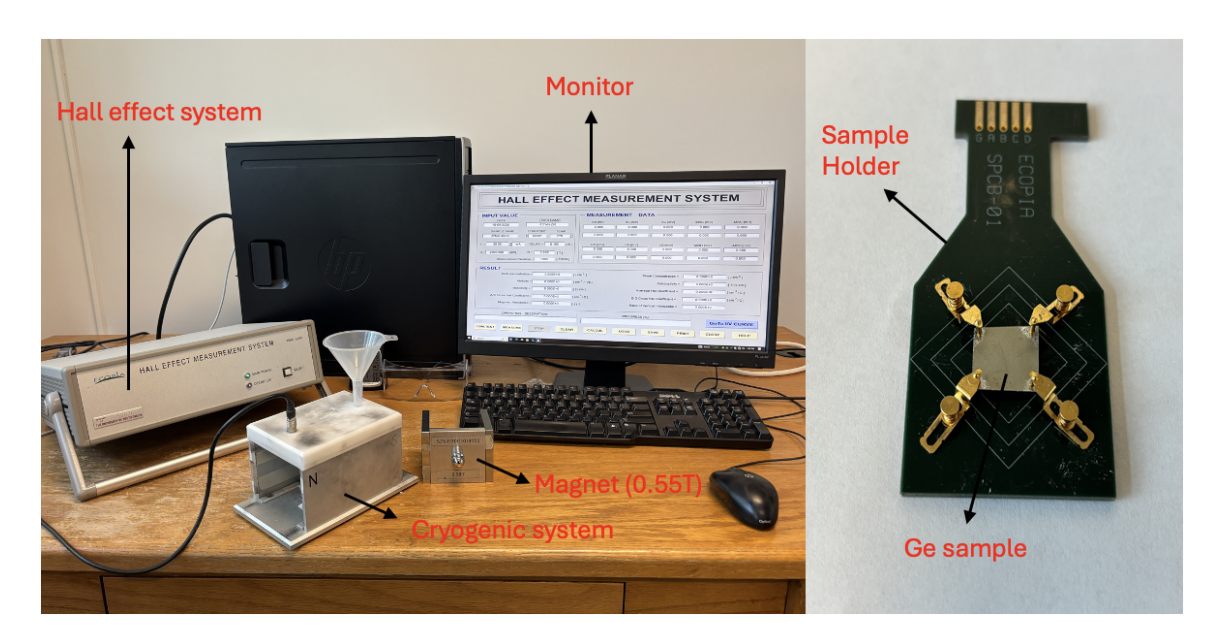


Figure 5. Ecopia HMS-3000 Hall-effect measurement system at USD used to determine electrical properties and net impurity concentrations of HPGe samples at 77 K.

where C is the impurity concentration in the solid, C_0 is the initial impurity concentration in the melt, g is the fraction of the melt that has solidified (obtained from the crystal mass), and K_{eff} is the effective segregation coefficient. Taking the natural logarithm of Eq. (3.1) gives

$$\ln C = (K_{\text{eff}} - 1) \ln(1 - g) + \ln(K_{\text{eff}} C_0). \tag{3.2}$$

Thus, a plot of $\ln C$ versus $\ln(1-g)$ should yield a straight line whose slope is $(K_{\text{eff}}-1)$ and whose intercept is $\ln(K_{\text{eff}}C_0)$. For each dopant region, the experimental data were fitted using a least-squares linear regression to obtain the slope and intercept, from which we extract the effective segregation coefficient K_{eff} and the corresponding initial impurity concentration C_0 .

4 Results and Discussion

The equilibrium distribution coefficient K_0 is defined as the ratio of the impurity concentration in the solid to that in the liquid under equilibrium conditions, $K_0 = C/C_0$, where C and C_0 are the solute concentrations in the solid and liquid phases, respectively. Traditionally, K_0 values are obtained from phase diagrams via the relative slopes of the solidus and liquidus lines. Approaching this ideal distribution in practice requires efficient solute mixing in the melt, controlled by growth rate, crystal rotation and impurity diffusivity.

Table 1. Equilibrium segregation coefficients K_0 for common impurities in germanium, defined as the ratio of impurity concentration in the solid to that in the liquid under equilibrium conditions [38].

Impurity	В	Al	Ga	P	Al-O complex
K_0	17	0.073	0.087	0.080	~ 1

In real CZ growth, non-equilibrium effects such as melt convection, RF-coil stirring and axial/radial thermal gradients cause deviations from these equilibrium values. The relevant quantity for detector-grade crystal pulling is therefore the effective segregation coefficient K_{eff} , which embeds the actual hydrodynamic and thermal conditions. The equilibrium coefficients K_0 for the dominant impurities in Ge, reported by Trumbore [38], are summarized in Table 1.

Photo-thermal ionization spectroscopy (PTIS) performed at 7 K on the HPGe crystals grown at USD confirms the presence of the primary shallow-level impurities—B, Al, Ga, and P—together with Al–O complexes and hydrogen—oxygen—related defect centers. The stronger PTIS response observed in the dark (blue curve), relative to the illuminated spectrum (red curve) in Figure 5 from [26], indicates that these centers undergo efficient photo-ionization at cryogenic temperatures, consistent with their behavior as shallow states whose bound carriers are readily depleted under light exposure. The simultaneous observation of donor, acceptor, and complex-related transitions further demonstrates that the material contains a combination of compensating impurities rather than a single dominant species. PTIS is highly sensitive to impurity species, but does not directly yield absolute concentrations; the relative contributions of the individual dopants to the net carrier density therefore require complementary electrical measurements [26].

In this work, we determine the effective segregation coefficients of B, Al+Ga and P in a CZ-grown HPGe crystal using the impurity-distribution formalism described in Sec. 3.1. Bulk impurity concentrations at each longitudinal position were obtained from Hall-effect measurements at 77 K, and the resulting profile is shown in Fig. 6. The crystal exhibits p-type behavior from 1.5 cm to 15 cm along its length and becomes n-type beyond 15.5 cm. A narrow region between 15 cm and 15.5 cm shows sharp compensation between acceptor (B, Al, Ga) and donor (P) impurities, resulting in the formation of a p-n junction.

4.1 Boron and Phosphorus Segregation

The segregation behavior of boron and phosphorus is quantified in the $\ln C$ versus $\ln(1-g)$ plots shown in Figs. 7 and 8. For B, twelve data points from the 2–9 cm region yield a positive slope in the $\ln C - \ln(1-g)$ plane, indicating that boron is preferentially incorporated into the solid. For P, eleven data points from the 16.5–21.5 cm region produce a negative slope, consistent with P remaining predominantly in the melt.

In both cases, a least-squares linear regression was applied to extract the effective segregation coefficient, where the slope corresponds to $(K_{\text{eff}} - 1)$ and the intercept to $\ln(K_{\text{eff}}C_0)$. The B and P fits yield coefficients of determination $R^2 = 0.85$ and $R^2 = 0.93$, respectively, demonstrating good agreement with the expected segregation behavior.

From these fits, the effective segregation coefficients and initial melt concentrations are

$$K_{\text{eff}}^{(\text{B})} = 11.41 \pm 1.36,$$
 $C_0^{(\text{B})} = (4.25 \pm 0.06) \times 10^{11} \text{ cm}^{-3},$ $K_{\text{eff}}^{(\text{P})} = 0.17 \pm 0.07,$ $C_0^{(\text{P})} = (3.82 \pm 0.65) \times 10^{12} \text{ cm}^{-3}.$

4.2 Aluminum and Gallium Segregation

Determining separate K_{eff} values for Al and Ga from Hall data alone is challenging, because the crystal is strongly B-dominated up to about 15 cm, leading to a pronounced p-type region in which

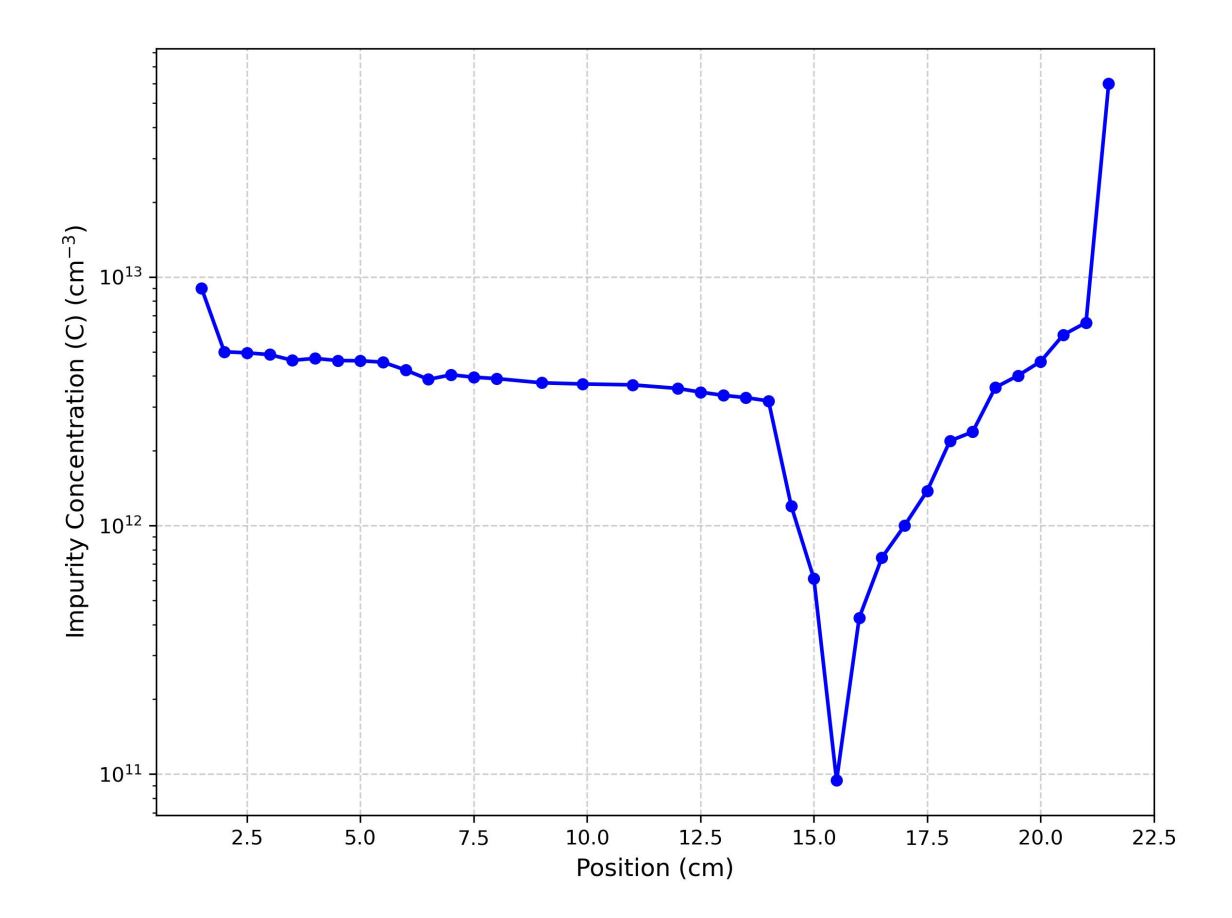


Figure 6. Longitudinal impurity concentration profile of the HPGe crystal grown at USD. The crystal is p-type from 1.5 cm to 15 cm and n-type beyond 15.5 cm. A sharp compensation region between 15.0 and 15.5 cm yields a p-n junction.

Al and Ga act as secondary acceptors. The Hall-measured net carrier concentration at position x_i ,

$$C_{\text{Nef}}(x_i) = C_R(x_i) + C_{AI}(x_i) + C_{Ga}(x_i) - C_P(x_i), \tag{4.1}$$

combines the contributions from all acceptors (B, Al, Ga) and the donor P [28]. To isolate the Al+Ga contribution, we first use the boron fit to estimate $C_B(x_i)$ and then subtract this from the net carrier concentration in the 9–15 cm region, where the P contribution is still small. This procedure yields an effective Al+Ga concentration profile.

Five data points from the 12–14 cm region were used to construct the $\ln C - \ln(1-g)$ plot for the combined Al+Ga impurity. The resulting linear fit, shown in Fig. 9, yields a negative slope of -0.33 with $R^2 = 0.90$. The corresponding effective segregation coefficient and initial melt concentration are

$$K_{\text{eff}}^{(\text{Al+Ga})} = 0.67 \pm 0.06, \qquad C_0^{(\text{Al+Ga})} = (5.47 \pm 0.09) \times 10^{12} \text{ cm}^{-3}.$$

The extracted K_{eff} and C_0 values for all three impurity classes are summarized in Table 2.

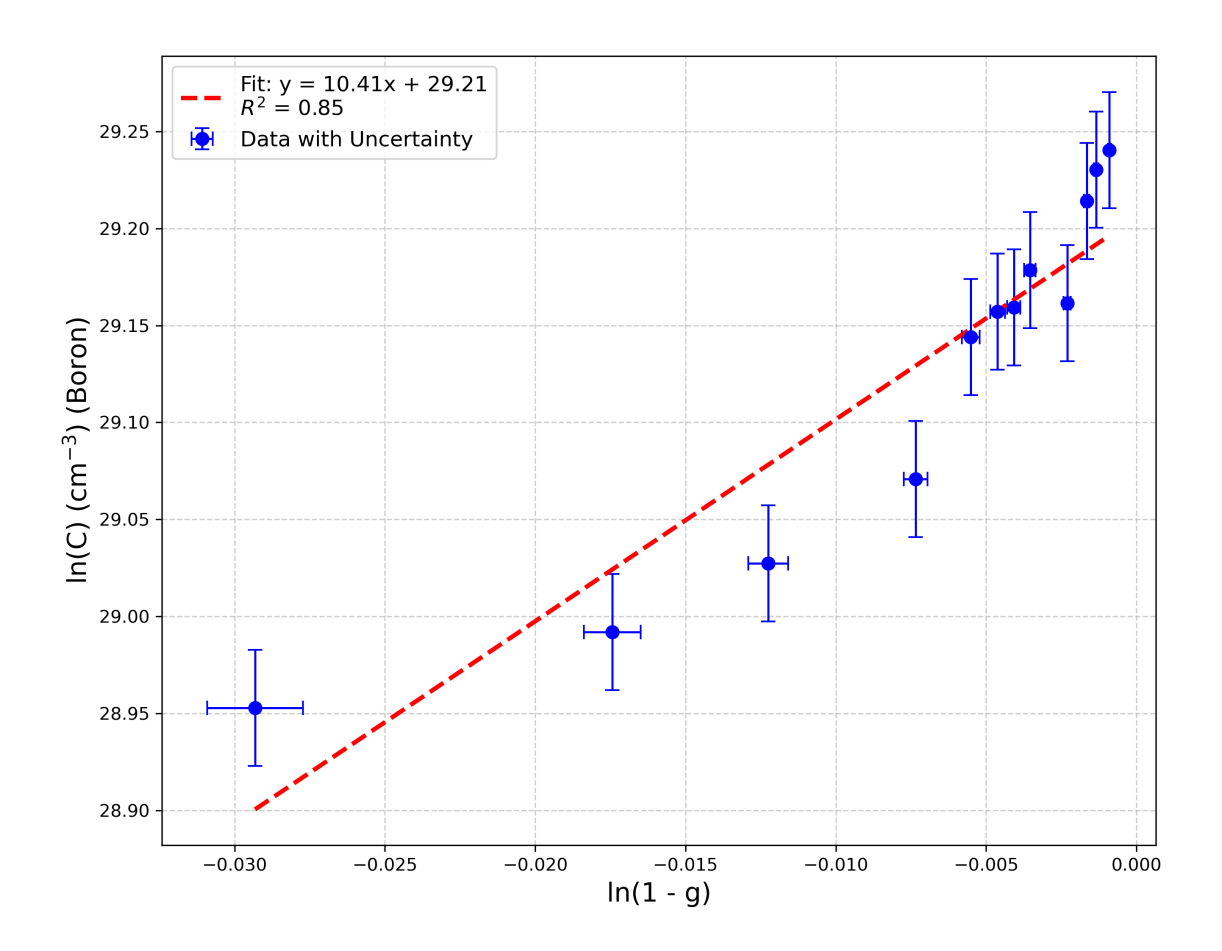


Figure 7. $\ln C$ versus $\ln(1-g)$ for boron, including uncertainties of 3.04% in the net carrier concentration and 5.36% in the solidified fraction g. Twelve data points from the 2–9 cm region were used. The linear regression yields a slope of 10.41 and $R^2 = 0.85$.

Table 2. Effective segregation coefficients K_{eff} and initial impurity concentrations C_0 for B, Al+Ga and P in the HPGe crystal grown at USD. Uncertainties correspond to 68% confidence intervals.

Impurity	$K_{ m eff}$	$C_0 ({\rm cm}^{-3})$
Boron	11.41 ± 1.36	$(4.25 \pm 0.06) \times 10^{11}$
Aluminum + Gallium	0.67 ± 0.06	$(5.47 \pm 0.09) \times 10^{12}$
Phosphorus	0.17 ± 0.07	$(3.82 \pm 0.65) \times 10^{12}$

4.3 Uncertainty Analysis

The Hall-effect measurement setup introduces a systematic uncertainty in the net carrier concentration of 3.04% for small, square-shaped samples [27]. The solidified fraction g is derived from the mass of each crystal segment and carries additional uncertainty due to cutting and positioning. A positional deviation of about 1 mm along the boule, stemming from diamond-wire saw alignment and operator variability, translates into a thickness and mass uncertainty that varies with crystal diameter.

For B, where the crystal diameter changes most significantly across the measured regions,

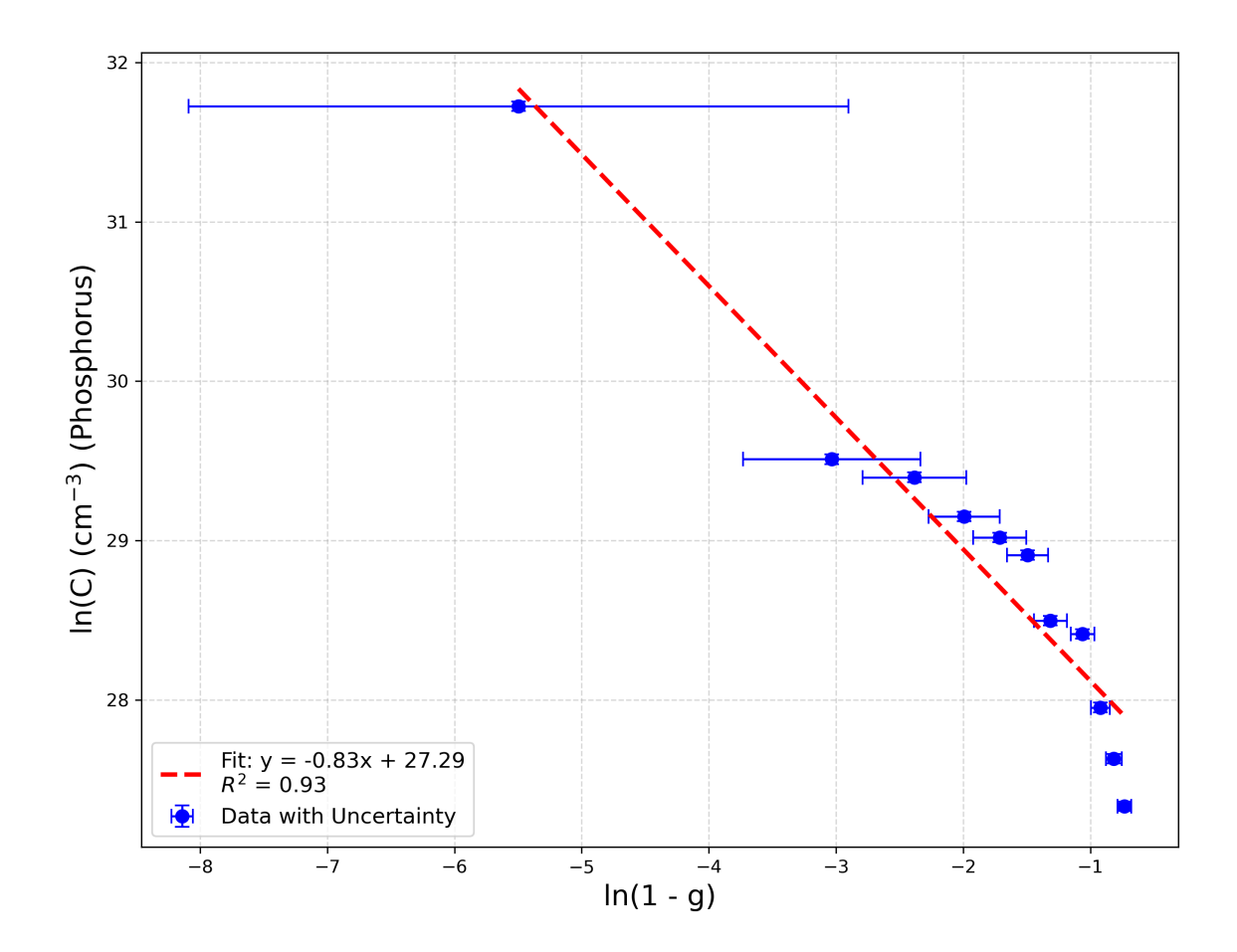


Figure 8. $\ln C$ versus $\ln(1-g)$ for phosphorus, including uncertainties of 3.04% in the net carrier concentration and 5.10% in g. Eleven data points from the 16.5–21.5 cm region were used. The linear regression yields a slope of -0.83 and $R^2 = 0.93$.

the mass differences associated with a 1 mm positional shift were estimated to be 0.29 g (1.5–2.5 cm), 0.72 g (3–5 cm), 2.02 g (5.5–7.5 cm) and 5.70 g (8–9 cm). These correspond to an average mass-related uncertainty of 5.36%. For Al+Ga and P, the crystal diameter is more uniform, and the mass variation over a 1 mm shift is approximately 70 g, giving an average uncertainty of 5.10%.

Uncertainties in $K_{\rm eff}$ and C_0 were obtained via residual analysis of the linear fits in the $\ln C - \ln(1-g)$ plane. Residuals were defined as the differences between measured and model-predicted $\ln C$ values, and the scatter was quantified through the standard errors of the slope and intercept. These errors were then propagated to $K_{\rm eff}$ and C_0 , yielding the 68% confidence intervals reported in Table 2.

4.4 Comparison with BPS Model and Literature

The classic Burton–Prim–Slichter (BPS) model [32] provides an approximate expression for the effective segregation coefficient:

$$K_{\text{eff}} = \frac{K_0}{K_0 + (1 - K_0) \exp(-f\delta/D)},$$
(4.2)

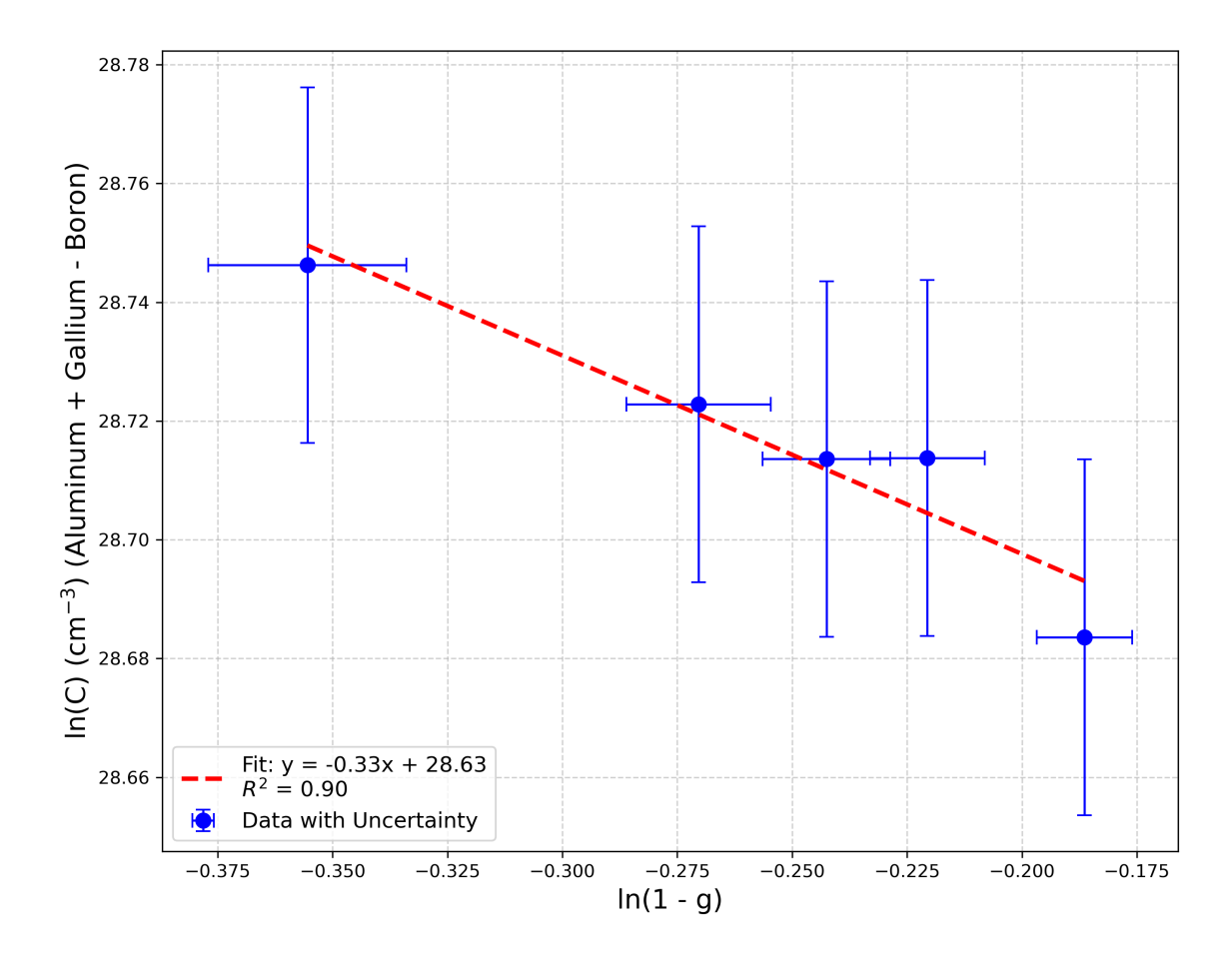


Figure 9. In *C* versus $\ln(1-g)$ for the combined Al+Ga impurity, including uncertainties of 3.04% in the net carrier concentration and 5.10% in *g*. The Al+Ga concentration is obtained by subtracting the B contribution from the Hall-measured net carrier density. Five data points from the 12–14 cm region were used. The fit yields a slope of -0.33 and $R^2 = 0.90$.

where K_0 is the equilibrium segregation coefficient, D is the impurity diffusion coefficient in the melt, δ is the solute boundary-layer thickness, and f is the crystal growth rate. The boundary-layer thickness is given by

$$\delta = 1.6 D^{1/3} v^{1/6} \omega^{-1/2}, \tag{4.3}$$

where $v = \mu/\rho$ is the kinematic viscosity of molten Ge $(1.35 \times 10^{-3} \, \text{cm}^2 \, \text{s}^{-1})$, and ω is the crystal rotation rate. The impurity diffusion coefficients in molten Ge span a range of values: for B and Ga, $D \approx 3 \times 10^{-4} \, \text{and} \, 7.2 \times 10^{-5} \, \text{cm}^2 \, \text{s}^{-1}$ [40, 41], while for P and Al, $D \approx 5 \times 10^{-5} \, \text{and} \, 6 \times 10^{-5} \, \text{cm}^2 \, \text{s}^{-1}$ [42–44]. For the combined Al+Ga impurity, we use the averages of their diffusion coefficients and K_0 values.

Using Eq. (4.3), we obtain diffusion boundary-layer thicknesses of 0.063 cm, 0.038 cm and 0.034 cm for B, Al+Ga and P, respectively. Inserting these into Eq. (4.2) with a rotation rate of 3 rpm and the K_0 and D values above yields approximate BPS-based effective segregation coefficients of $K_{\text{eff}}^{(\text{BPS})} \approx 6.12$ for B, 0.10 for Al+Ga, and 0.11 for P.

These estimates are broadly consistent with the trends observed in our data $(K_{\text{eff}}^{(B)} \gg 1, K_{\text{eff}}^{(P)} <$

1), but differ quantitatively, particularly for Al+Ga, where our measured $K_{\rm eff}^{\rm (Al+Ga)}=0.67\pm0.06$ is substantially larger than the BPS estimate. Part of this discrepancy likely arises from the sensitivity of the BPS model to input parameters that are themselves uncertain, including D, K_0 and the exact hydrodynamic conditions in the melt. In addition, Al- and Ga-related complexes (e.g. Al–O) and incomplete melt homogenization can alter the effective segregation behavior relative to the idealized assumptions of the BPS framework.

Earlier experimental work also reports a spread in effective segregation coefficients. Burton *et al.* [32] obtained approximate K_{eff} values of 0.12 for P and 0.10 for Ga in Ge. Edwards [45] later measured $K_{\text{eff}} \approx 12.2$ for B, emphasizing that slow growth and high rotation rates favor values closer to K_0 . Bridgers and co-workers [46] reported a wider range for B (2.2–17.4), with higher values correlated with increased growth rates, underscoring the impact of non-equilibrium conditions.

Within this broader context, the present results show internally consistent K_{eff} values across all three impurity classes for a single crystal grown under well-documented conditions. They thus provide a more tightly constrained benchmark for impurity segregation in detector-grade HPGe grown by the Czochralski method and offer practical input for tuning growth parameters to achieve desired longitudinal impurity profiles.

5 Conclusion

High-purity germanium (HPGe) crystals were successfully grown at USD using the Czochralski technique, with diameters ranging from ~ 8 cm near the shoulder to ~ 11 cm toward the tail. For the first time at USD, a detector-grade HPGe crystal was longitudinally sectioned into 37 segments, enabling high-resolution mapping of net impurity concentrations via Hall-effect measurements at 77 K. Using a standard impurity-distribution model and ln–ln linear regression, we extracted effective segregation coefficients for boron, combined aluminum and gallium, and phosphorus of $11.41\pm1.36, 0.67\pm0.06$, and 0.17 ± 0.07 , respectively. The corresponding initial melt concentrations were $(4.25\pm0.06)\times10^{11}$, $(5.47\pm0.09)\times10^{12}$, and $(3.82\pm0.65)\times10^{12}$ cm⁻³.

These values provide a quantitative, internally consistent picture of impurity segregation under realistic HPGe detector-growth conditions at USD and complement classical Burton–Prim–Slichter estimates and prior literature. The methodology demonstrated here establishes a reproducible framework for linking growth parameters to longitudinal impurity profiles and will guide optimization of zone refining and CZ pulling to increase the yield and uniformity of detector-grade HPGe. In turn, this supports the development of next-generation low-background HPGe detectors for rare-event physics applications, including dark-matter and neutrinoless double-beta decay searches.

Acknowledgments

This work was supported in part by NSF OISE 1743790, NSF PHYS 2117774, NSF OIA 2427805, NSF PHYS 2310027, NSF OIA 2437416, DOE DE-SC0024519, DE-SC0004768, and a research center supported by the State of South Dakota. [20]

Author Contributions

The conceptualization and methodology were developed by S. Chhetri, D.-M. Mei and S. Bhattarai. Crystal growth was performed by S. Chhetri, S. Bhattarai, N. Budhathoki, A. Warren, K.-M. Dong. Sample preparation was supported by S. A. Panamaldeniya, and A. Prem. Experimental measurements were carried out by S. Chhetri. Data curation, formal analysis, and the original draft were completed by S. Chhetri. Visualization and manuscript review were carried out by S. Chhetri and D.-M. Mei. Project supervision, resource provision, and funding acquisition were led by D.-M. Mei. All authors contributed to the development of the study and approved the final manuscript.

References

- [1] A. Anderson, J. Conrad, E. Figueroa-Feliciano, K. Scholberg and J. Spitz, *Coherent neutrino scattering in dark matter detectors*, *Physical Review D—Particles*, *Fields*, *Gravitation*, and *Cosmology* **84** (2011) 013008.
- [2] W.-Z. Wei, D.-M. Mei and C. Zhang, Cosmogenic activation of germanium used for tonne-scale rare event search experiments, Astroparticle Physics **96** (2017) 24.
- [3] M. Agostini, M. Allardt, E. Andreotti, A. Bakalyarov, M. Balata, I. Barabanov et al., *Production, characterization and operation of 76 ge enriched bege detectors in gerda: Gerda collaboration, The European Physical Journal C* **75** (2015) 39.
- [4] M. Agostini, A. Bakalyarov, M. Balata, I. Barabanov, L. Baudis, C. Bauer et al., *Probing majorana neutrinos with double-β decay, Science* **365** (2019) 1445.
- [5] R. Agnese, A. Anderson, T. Aramaki, W. Baker, D. Balakishiyeva, S. Banik et al., *Nuclear-recoil* energy scale in cdms ii silicon dark-matter detectors, *Nuclear Instruments and Methods in Physics* Research Section A: Accelerators, Spectrometers, Detectors and Associated Equipment **905** (2018) 71.
- [6] Y. Kermaidic and D. Radford, 76ge detector r&d strategy for legend, in XXVIII International Conference on Neutrino Physics and Astrophysics, p. 5, 2018.
- [7] C.E. Aalseth, P.S. Barbeau, J. Colaresi, J. Collar, J. Diaz Leon, J.E. Fast et al., *Cogent: A search for low-mass dark matter using p-type point contact germanium detectors, Physical Review D—Particles, Fields, Gravitation, and Cosmology* **88** (2013) 012002.
- [8] G. Angloher, M. Bauer, I. Bavykina, A. Bento, A. Brown, C. Bucci et al., *Commissioning run of the cresst-ii dark matter search*, *Astroparticle Physics* **31** (2009) 270.
- [9] C.E. Aalseth, P. Barbeau, J. Colaresi, J. Collar, J. Diaz Leon, J.E. Fast et al., Search for an annual modulation in a p-type point contact germanium dark matter detector, Physical Review Letters 107 (2011) 141301.
- [10] H. Klapdor-Kleingrothaus, A. Dietz and I. Krivosheina, *Status of evidence for neutrinoless double beta decay*, in *Dark Matter in Astro-and Particle Physics: Proceedings of the International Conference DARK 2002, Cape Town, South Africa, 4–9 February 2002*, pp. 367–403, Springer, 2002.
- [11] R. Agnese, T. Aralis, T. Aramaki, I. Arnquist, E. Azadbakht, W. Baker et al., *First dark matter constraints from a supercdms single-charge sensitive detector*, *Physical review letters* **121** (2018) 051301.
- [12] E. Armengaud, C. Augier, A. Benoît, A. Benoît, L. Bergé, J. Billard et al., *Searching for low-mass dark matter particles with a massive ge bolometer operated above ground, Physical Review D* **99** (2019) 082003.

- [13] L. Yang, H. Li, Q. Yue, H. Ma, K. Kang, Y. Li et al., Search for light weakly-interacting-massive-particle dark matter by annual modulation analysis with a point-contact germanium detector at the china jinping underground laboratory, Physical Review Letters 123 (2019) 221301.
- [14] G. Collaboration, M. Agostini, A. Bakalyarov, M. Balata, I. Barabanov, L. Baudis et al., *Upgrade for phase ii of the gerda experiment, The European Physical Journal C* **78** (2018) 388.
- [15] S. Alvis, I. Arnquist, F. Avignone III, A. Barabash, C. Barton, V. Basu et al., Search for neutrinoless double-β decay in ge 76 with 26 kg yr of exposure from the majorana demonstrator, Physical Review C 100 (2019) 025501.
- [16] C. Romo-Luque, Results of the legend-200 experiment in the search for neutrinoless double beta decay, arXiv preprint arXiv:2508.18573 (2025).
- [17] R. Agnese, A. Anderson, T. Aralis, T. Aramaki, I. Arnquist, W. Baker et al., *Low-mass dark matter search with cdmslite*, *Physical Review D* **97** (2018) 022002.
- [18] J. Aalbers, D. Akerib, C. Akerlof, A. Al Musalhi, F. Alder, A. Alqahtani et al., *First dark matter search results from the lux-zeplin (lz) experiment, Physical review letters* **131** (2023) 041002.
- [19] E. Aprile, K. Abe, F. Agostini, S. Ahmed Maouloud, L. Althueser, B. Andrieu et al., *First dark matter search with nuclear recoils from the xenonnt experiment, Physical review letters* **131** (2023) 041003.
- [20] D.-M. Mei, N. Budhathoki, S. Panamaldeniya, K.-M. Dong, S. Bhattarai, A. Warren et al., *Probing low-mass dark matter from sub-mev to sub-gev with germanium-based quantum phononic spectroscopy, Physics of the Dark Universe* (2025) 102165.
- [21] D. Mei, S. Panamaldeniya, K. Dong, S. Bhattarai, N. Budhathoki and A. Warren, *Phonon-coupled hole-spin qubits in high-purity germanium: design and modeling of a scalable architecture, Quantum Science and Technology* **10** (2025) 045067.
- [22] D.-M. Mei, Z.-B. Yin and S. Elliott, *Cosmogenic production as a background in searching for rare physics processes*, *Astroparticle Physics* **31** (2009) 417.
- [23] W. Hansen, *High-purity germanium crystal growing*, *Nuclear Instruments and Methods* **94** (1971) 377.
- [24] E.E. Haller, W.L. Hansen and F.S. Goulding, *Physics of ultra-pure germanium*, *Advances in Physics* **30** (1981) 93.
- [25] G. Wang, M. Amman, H. Mei, D. Mei, K. Irmscher, Y. Guan et al., Crystal growth and detector performance of large size high-purity ge crystals, Materials Science in Semiconductor Processing 39 (2015) 54.
- [26] G. Yang, J. Govani, H. Mei, Y. Guan, G. Wang, M. Huang et al., *Investigation of influential factors on the purification of zone-refined germanium ingot, Crystal Research and Technology* **49** (2014) 269.
- [27] M.-S. Raut, H. Mei, D.-M. Mei, S. Bhattarai, W.-Z. Wei, R. Panth et al., *Characterization of high-purity germanium (ge) crystals for developing novel ge detectors, Journal of Instrumentation* **15** (2020) T10010.
- [28] S. Bhattarai, D. Mei, N. Budhathoki, K. Dong and A. Warren, *Investigating influential parameters for high-purity germanium crystal growth*, *Crystals* **14** (2024) 177.
- [29] E.E. Haller, W. Hansen, G. Hubbard and F. Goulding, *Origin and control of the dominant impurities in high-purity germanium*, *IEEE Transactions on Nuclear Science* **23** (2007) 81.

- [30] B. Depuydt, A. Theuwis and I. Romandic, Germanium: From the first application of czochralski crystal growth to large diameter dislocation-free wafers, Materials Science in Semiconductor Processing 9 (2006) 437.
- [31] D. Mei, R. Mukund, W. Wei, R. Panth, J. Liu, H. Mei et al., Impact of charge trapping on the energy resolution of ge detectors for rare-event physics searches, Journal of Physics G: Nuclear and Particle Physics 47 (2020) 105106.
- [32] J. Burton, R. Prim and W. Slichter, *The distribution of solute in crystals grown from the melt. part i. theoretical, The journal of chemical physics* **21** (1953) 1987.
- [33] R. Hall, Segregation of impurities during the growth of germanium and silicon, The Journal of Physical Chemistry 57 (1953) 836.
- [34] G. Wang, H. Mei, D. Mei, Y. Guan and G. Yang, *High purity germanium crystal growth at the university of south dakota*, in *Journal of Physics: Conference Series*, vol. 606, p. 012012, IOP Publishing, 2015.
- [35] S. Bhattarai, R. Panth, W.-Z. Wei, H. Mei, D.-M. Mei, M.-S. Raut et al., *Investigation of the electrical conduction mechanisms in p-type amorphous germanium electrical contacts for germanium detectors in searching for rare-event physics, The European Physical Journal C* **80** (2020) 950.
- [36] X.-H. Meng, G.-J. Wang, M.-D. Wagner, H. Mei, W.-Z. Wei, J. Liu et al., Fabrication and characterization of high-purity germanium detectors with amorphous germanium contacts, Journal of Instrumentation 14 (2019) P02019.
- [37] G. Yang, Y. Guan, F. Jian, M. Wagner, H. Mei, G. Wang et al., *Zone refinement of germanium crystals*, in *Journal of Physics: Conference Series*, vol. 606, p. 012014, IOP Publishing, 2015.
- [38] F.A. Trumbore, Solid solubilities of impurity elements in germanium and silicon, Bell System Technical Journal **39** (1960) 205.
- [39] W.G. Pfann, Principles of zone-melting, Jom 4 (1952) 747.
- [40] T. Taishi, Y. Murao, Y. Ohno and I. Yonenaga, Segregation of boron in germanium crystal, Journal of Crystal Growth 311 (2008) 59.
- [41] A. Subramanian, N. Abrosimov, A. Gybin, C. Guguschev, U. Juda, A. Fiedler et al., *Investigation of doping processes to achieve highly doped czochralski germanium ingots, Journal of Electronic Materials* **52** (2023) 5178.
- [42] H. Kodera, Constitutional supercooling during the crystal growth of germanium and silicon, Japanese Journal of Applied Physics 2 (1963) 527.
- [43] M. Becker, F. Kargl and A. Bührig-Polaczek, *Solidification kinetics in al-cu and al-ge alloys investigated by in-situ x-ray radiography*, Tech. Rep. Fachgruppe für Materialwissenschaft und Werkstofftechnik (2017).
- [44] M. Becker, S. Klein and F. Kargl, *Free dendritic tip growth velocities measured in al-ge, Physical Review Materials* **2** (2018) 073405.
- [45] W. Edwards, *The distribution coefficient of boron in germanium, Journal of The Electrochemical Society* **117** (1970) 1062.
- [46] H.E. Bridgers and E. Kolb, *Distribution coefficient of boron in germanium*, *Journal of Chemical Physics* **25** (1956) 648.